Available online at www.sciencedirect.com
SCIENCE DIRECT®
Biomaterials 27 (2006) 2095–2113
Biomaterials
www.elsevier.com/locate/biomaterials

Fracture length scales in human cortical bone: The necessity of nonlinear fracture models

Q.D. Yang[a,*], Brian N. Cox[a], Ravi K. Nalla[b], R.O. Ritchie[b]

[a]*Rockwell Scientific Co., LLC, 1049 Camino Dos Rios, Thousand Oaks, CA 91360, USA*
[b]*Materials Sciences Division, Lawrence Berkeley National Laboratory and University of California, Berkeley, CA 94720, USA*

Received 26 April 2005; accepted 26 September 2005
Available online 4 November 2005

Abstract

Recently published data for fracture in human humeral cortical bone are analyzed using cohesive-zone models to deal with the nonlinear processes of material failure. Such models represent the nonlinear deformation processes involved in fracture by cohesive tractions exerted by the failing material along a fracture process zone, rather than attributing all damage to a process occurring at a single point, as in conventional linear-elastic fracture mechanics (LEFM). The relationship between the tractions and the net displacement discontinuity across the process zone is hypothesized to be a material property for bone. To test this hypothesis, the cohesive law was evaluated by analyzing published load vs. load-point displacement data from one laboratory; the calibrated law was then used to predict similar data taken for a different source of bone using a different specimen geometry in a different laboratory. Further model calculations are presented to illustrate more general characteristics of the nonlinear fracture of bone and to demonstrate in particular that LEFM is not internally consistent for all cases of interest. For example, the fracture toughness of bone deduced via LEFM from test data is not necessarily a material constant, but will take different values for different crack lengths and test configurations. LEFM is valid when the crack is much longer than a certain length scale, representative of the length of the process zone in the cohesive model, which for human cortical bone ranges from 3 to 10 mm. Since naturally occurring bones and the specimens used to test them are *not* much larger than this dimension for most relevant orientations, it is apparent that only nonlinear fracture models can give an internally consistent account of their fracture. The cohesive law is thus a more complete representation of the mechanics of material failure than the single-parameter fracture toughness and may therefore provide a superior measure of bone quality. The analysis of fracture data also requires proper representation of the approximately orthotropic elasticity of the bone specimen; if the specimen is incorrectly assumed to be isotropic, the initial measured compliance cannot be reproduced to within a factor of four and the fracture toughness deduced from the measured work of fracture will be overestimated by ~30%.

Keywords: Cortical bone; Fracture; Toughness; Cohesive zone

1. Introduction

It is well known that the deterioration in the quantity and quality of bone in the human musculoskeletal system with aging and disease results in severely increased risks of bone fracture [1]; for the very elderly, this can lead to significant mortality [2]. In cortical bone, such aging results in the accumulation of microdamage, invariably in the form of microcracks [3], and a definitive decay in the inherent resistance to fracture [4–11]. Whereas the precise links between the increasing levels of diffuse microdamage and increased fracture risk remain unclear, the degradation in the fracture resistance, quantified in terms of the toughness, is undisputed. In this work, we consider how the toughness of bone should be evaluated. To date, most assessments have involved linear-elastic fracture mechanics (LEFM) analyses which yield a single-valued fracture toughness. However, we show that the complexity of fracture in cortical bone, over dimensions comparable to those in the human skeleton, warrants a more detailed (nonlinear) evaluation of such fracture instability.

*Corresponding author. Tel.: +1 805 373 4316; fax: +1 805 373 4017.
E-mail address: qyang@rwsc.com (Q.D. Yang).

0142-9612/$ - see front matter © 2005 Elsevier Ltd. All rights reserved.
doi:10.1016/j.biomaterials.2005.09.040

Nomenclature

a	crack length
a_0	length of traction-free crack
b_{ij}	Voigt elastic constants
c_0	length of initial notch plus notch extension
d_1, d_2	specimen dimensions
δ	small quantity
Δ	load-point displacement
E, E_i	Young's moduli
E'	combination of elastic constants
ε_{ij}	component of strain
$\varepsilon_{ij}^{(c)}$	critical value of strain
$\varepsilon_{ij}^{(p)}$	component of plastic strain
f	fitting function
G_i	strain energy release rates, $i = \mathrm{I}, \mathrm{II}, \mathrm{III}$
G_{ic}	critical value of G_i, $i = \mathrm{I}, \mathrm{II}, \mathrm{III}$
h	specimen height
K_i	stress-intensity factors, $i = \mathrm{I}, \mathrm{II}, \mathrm{III}$
K_{ic}	critical value of K_i, $i = \mathrm{I}$, II, III
K_b	reduction of stress-intensity factor due to bridging
$K_R(a)$	apparent critical stress-intensity factor at crack length a
λ_b	length of bridging or process zone
l_{ch}	characteristic length of traction-displacement law
LEFM	linear-elastic fracture mechanics
μ, μ_{ij}	engineering shear moduli
N	elapsed load cycles
ν, ν_{ij}	Poisson's ratios
w_b	half-width of bridging or process zone
w_m	maximum value of w_b
P	load per unit thickness
$\boldsymbol{p}$	vector (p_1, p_2, p_3) of crack tractions per unit thickness
p_c, p_0	parameters of traction-displacement law
s_1	initial slope of load vs. load-point displacement data
σ_{ij}	component of stress
t	specimen thickness
t_g	minimum thickness of a grooved $C(T)$ specimen
τ	time
$\boldsymbol{u}$	crack displacement vector (u_1, u_2, u_3)
u_c, u_0	parameters of traction-displacement law
$\boldsymbol{x}$	spatial coordinates (x_1, x_2, x_3)
w	specimen width
W_i	total and partial values of the work of fracture, $i =$ total, tip, brid
Y	a constant

2. Limitations of prior fracture models of bone

2.1. Traditional engineering view of constitutive/fracture behavior of cortical bone

Cortical bone is a natural composite consisting of an organic matrix of ~90% type-I collagen with 10% other organic materials (mainly proteins) together with a mineral phase of hydroxyapatite [12]. This is similar for all collagen-based mineralized tissues, although the distribution and ratio of the organic and mineral phases varies with the function of the particular tissue; for human cortical bone this ratio is roughly 1:1 by volume and 1:3 by weight [13]. Composition and structure, however, vary with such factors as skeletal site, age, sex, physiological function and mechanical loading, making bone a very heterogeneous material, with the need for vascularization adding to the complexity of the tissue. Its structure is hierarchical and thus can be considered at several dimensional scales. At the nanoscale, bone is composed of type-I mineralized collagen fibers (up to 15 μm in length, 50–70 nm in diameter, and bundled together) made up of a regular, staggered arrangement of collagen molecules. These fibers are bound and impregnated with carbonated apatite nanocrystals (tens of nanometers in length and width, 2–3 nm in thickness) [12] and are further organized at microstructural length-scales into a lamellar structure with adjacent lamellae being 3–7 μm thick [14]. Generally oriented along the long axis of bones are the secondary osteons [15], which are central to the remodeling process to repair damage in vivo. They are composed of large (~50–90 μm diameter) vascular channels surrounded by circumferential lamellar rings, with so-called "cement lines" at the outer boundary.

To date, mechanical descriptions of fracture in cortical bone have, with only a few recent exceptions, been presented via LEFM, with the toughness deemed to be a material constant and identified with a point process at the crack tip (e.g., [11,16–18]); any inelastic behavior is presumed to be limited to a small near-tip region. Under such small-scale yielding conditions, the stress and displacement fields local to the tip of a pre-existing crack are described by the stress-intensity factor, K_i, and resistance to fracture, or the fracture toughness, is defined as the critical stress-intensity value, K_{ic}, at the onset of unstable fracture. [1] These K_{ic} values have been assumed to

[1] K_i can be defined for three modes of loading: $i = \mathrm{I}$ (mode I tensile-opening), II (mode II shear) and III (mode III anti-plane shear). For each of these modes, a corresponding fracture toughness, K_{ic}, may be defined as the critical value of K_i at fracture instability, i.e., when $K_i = Y\sigma_{app}(\pi a)^{1/2} = K_{ic}$, where σ_{app} is the applied stress, a is the crack length, and Y is a function (of order unity) of crack size and geometry. Alternatively, the toughness can be expressed as a critical value of the strain-energy release rate, G_c, defined as the change in potential energy per unit increase in crack area. For an isotropic material, $G_c = K_{Ic}^2/E' + K_{IIc}^2/E' + K_{IIIc}^2/2\mu$, where $E' = E$ in plane stress and $E' = E/(1-\nu^2)$ in plane strain, with E Young's modulus and ν Poisson's ratio, and μ is the engineering shear modulus. See text for amendments necessary for an orthotropic material.

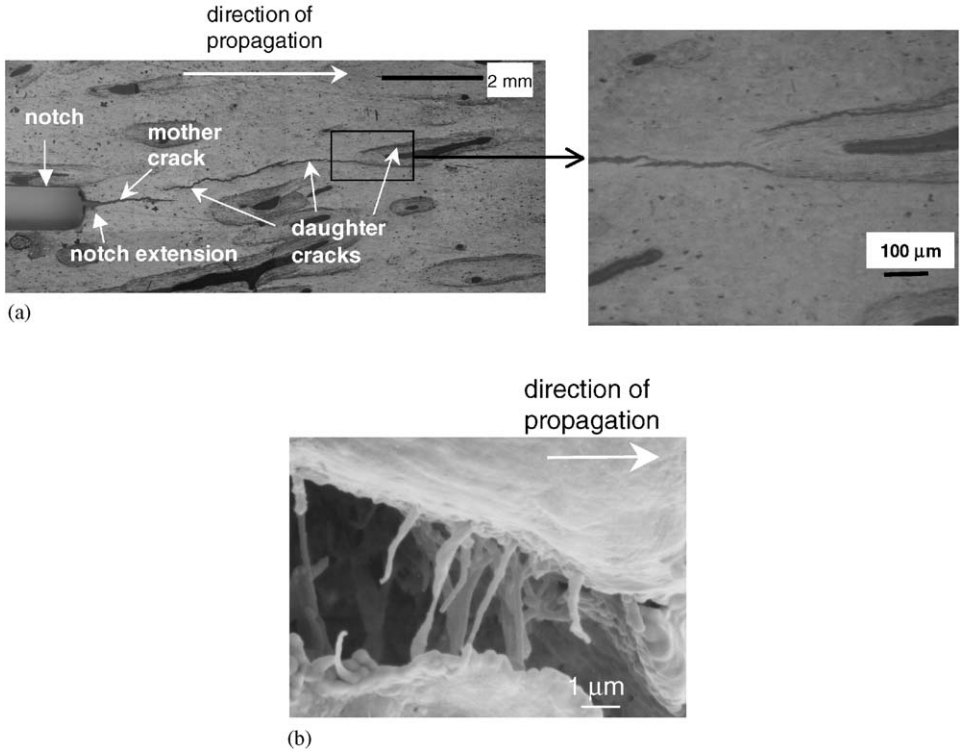

Fig. 1. (a) An optical micrograph of a crack in 34-year-old human cortical bone. Note the formation of daughter cracks and corresponding uncracked ligaments [27]. (b) Bridging by collagen fibrils in the wake of a crack in human cortical bone [27].

be material constants, although the toughness is known to depend on various factors including age, disease, loading mode, and the anatomical location and orientation within the bone [9,10,12,19–21]. The anisotropic properties can be related to microstructural anisotropy, in particular to the orientation of osteon structures, collagen fibrils, and apatite mineral platelets. Specifically, cortical bone is typically a factor of two tougher in the transverse orientation, i.e., where the crack must cut the osteons, largely because cracks tend to deflect along the cement lines (osteon/bone–matrix interfaces) [21,22]. Curiously, however, given the highly heterogeneous and hierarchical structure and morphology of bone, the great majority of studies to date do not entertain the prospect of spatial non-uniformity in continuum or fracture properties. An outstanding problem is therefore to model heterogeneity in mechanical properties (elasticity, viscosity, etc.), over all scales that are shown to be relevant by detailed experiments, in terms of variations in the composition and morphology of the bone.

2.2. Evidence for nonlinear fracture (bridged cracks) in cortical bone

Recently, this LEFM paradigm has been challenged in a series of papers that have recognized that the fracture of bone cannot be characterized by a single-valued toughness, rather that behavior must be described in terms of a so-called crack-resistance curve (*R*-curve), where the driving force for fracture increases with crack extension [23–25]. This phenomenon can arise when toughening mechanisms act in the crack wake [26]. Such a notion is consistent with recent studies in cortical bone that show that fracture occurs via a complex system of mother–daughter cracks; microcracks associated with the osteon structures [24] form ahead of, and around, the primary crack and link back to it only after lands of intact material, a few to hundreds of micrometers in size, deform and break after further loading (Fig. 1a) [21,24,27]. In a single-crack idealization, such nonlinear processes are represented by a cohesive or bridging zone at the leading edge of the dominant crack; the nonlinear mechanisms continue to carry load in this zone, which would otherwise be available to drive the crack.

The total length, λ_b, of the nonlinear zone in the crack wake is a primary characteristic of the fracture process; in human cortical bone, the observed zone of bridging can be as large as $\lambda_b \sim 5$ mm [24,27]. As this is comparable to the cortical layer thickness, even in larger human bones such as the humerus or femur, the validity of LEFM for bone is questionable. When a fracture process zone is commensurate with the structure, large-scale bridging or yielding conditions apply and the fracture toughness is no longer a material constant [28–33]. For a single (mother) crack with a process zone, e.g., the crack-bridging zone of microcracks or daughter cracks in Fig. 1b, the critical applied (or measured) stress-intensity factor, K_c, depends on extrinsic factors such as the geometry and loading configuration,

because the contribution to toughening from bridging, K_b, depends on the crack length (e.g., [28,34,35]). In such cases, the fracture properties can only be correctly accounted for by determining the constitutive behavior of all the nonlinear crack wake mechanisms.

3. Nonlinear fracture model

3.1. The line-spring idealization

To account for these features in fracture data for cortical bone, nonlinear fracture formulations will be presented for the problem of a single dominant crack, around which microcracks or other nonlinear material events can occur within a nonlinear fracture process zone (Fig. 2a). The line-spring idealization [32,36–38] provides an accurate and simple formulation, in which the changes in the displacement fields around the crack due to a diffuse fracture process zone are collapsed into a displacement discontinuity existing across a surface (Fig. 2b). The vector displacement discontinuity, $2\boldsymbol{u}$, is defined as the net nonlinearity across the whole zone in the real material, i.e., for a plane problem in which the crack propagates in the x_1 direction along $x_3 = 0$:

$$u_i(x_1) = \int_0^{w_b(x_1)} \varepsilon_{i3}^{(p)}(x_1, x_3)\, dx_3, \quad (i = 1 \text{ or } 3), \tag{1}$$

where $2w_b(x_1)$ is the width of the nonlinear damage zone at position x_1, and $\varepsilon_{ij}^{(p)}$ is the plastic strain tensor, i.e., the strain in excess of that for linear, undamaged material under the same local stress state. The plastic strain is not necessarily uniform in the damage zone and may incorporate rate localization events such as microcracking.

Traction fields, $\boldsymbol{p}$, are imposed along the material surfaces that have become separated by the displacement discontinuity, to ensure that the stress in the material abutting the surfaces is identical to that expected in the nonlinear material (Fig. 2b). For problems with plane symmetry, the single dominant crack is thus represented as two domains: one traction-free ($0 \leqslant x_1 \leqslant a_0$; $\boldsymbol{p} = 0$) and one where line springs act ($a_0 \leqslant x_1 \leqslant a$; $\boldsymbol{p} \neq 0$). All the nonlinearity in the fracture problem is represented by the displacement discontinuity, $2\boldsymbol{u}$, and the nonlinear constitutive behavior of the material in the damage zone is subsumed in the relationship $\boldsymbol{p}(\boldsymbol{u})$, in which both opening and sliding displacements are possible. In the cases of plane symmetry studied here, $\boldsymbol{p}$ will denote the tractions per unit specimen thickness.

In many materials, the relationship $\boldsymbol{p}(\boldsymbol{u})$ proves to be a material constant, i.e., a fixed relation $\boldsymbol{p}(\boldsymbol{u})$ accounts for data from different types of test, even under conditions in which the deduced value of the fracture toughness is not constant but depends on the crack length or the specimen geometry [28,35]. However, other variables may influence $\boldsymbol{p}$ in bone, including loading rate (time, τ), elapsed cycles, N, and the biological state of the material (protein composition, chemical environment, hydration, etc.), which may be a function of position, $\boldsymbol{x}$. In the most general conditions, one expects a relation $\boldsymbol{p}(\boldsymbol{u}, \tau, N, \boldsymbol{x}, \ldots)$, whose true form remains a challenging topic for future research; but these effects are not evident in the data analyzed here.

3.2. Cohesive and bridged crack models

The leading edge of the nonlinear zone in the line-spring model, which lies at $x_1 = a$ in the plane symmetry

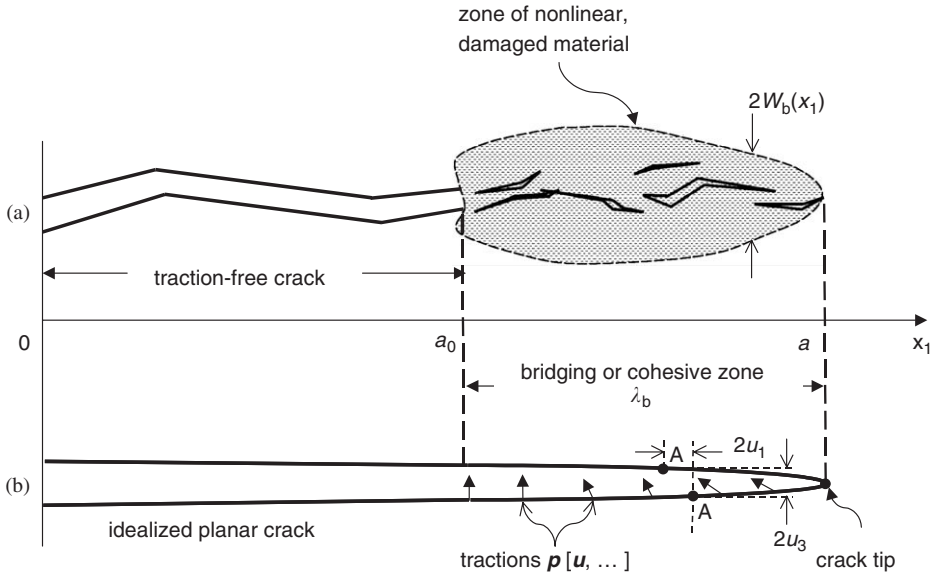

Fig. 2. Schematic of (a) discrete damage that has evolved into a single dominant crack with a diffuse crack tip damage zone and (b) the same system idealized as a planar crack with a bridging or cohesive zone. Tractions, $\boldsymbol{p}$, are shown acting on one surface only, but must also act in equal magnitude and opposite sense on the other surface. As suggested, the tractions can vary in direction and magnitude along the cohesive zone. The displacement discontinuity across the crack is exemplified by the points marked A, which were coincident prior to fracture.

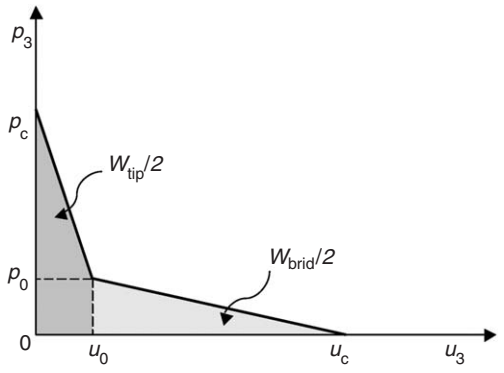

Fig. 3. A hypothetical cohesive traction law for a mode I cohesive zone.

conditions of Fig. 2, will be referred to in this paper as the crack tip, rather than the furthest progression of the traction-free domain ($x_1 = a_0$). The boundary condition imposed at the crack tip to close the fracture problem is taken to be that the stress-intensity factor at the crack tip should be zero and thus the stress components, σ_{33}, σ_{31}, and σ_{12} in the material immediately ahead of the crack tip ($x_1 = a + \delta$) approach the values $p_3(0)$, $p_1(0)$, and $p_2(0)$, respectively, as $\delta \to 0$. This closure condition is known as a *cohesive crack model*. This formulation is equivalent, mathematically and physically, to a bridged crack model in which a critical condition is imposed on the stress-intensity factors, K_I, K_{II}, and K_{III} (or equivalently on the strain-energy release rates, G_I, G_{II}, and G_{III}) at the crack tip, provided a traction-free crack domain ($0 \leqslant x_1 \leqslant a_0$) exists and is reasonably large [29,39]. Equivalence is accomplished by defining, in the cohesive crack model, a part of the traction law, $\boldsymbol{p}(\boldsymbol{u})$, that will contribute high traction values at small displacements $\boldsymbol{u}$, e.g., when $u_3 < u_0$ for a mode I crack (Fig. 3). This part of the cohesive law describes physical processes occurring relatively near to the crack tip ($x_1 \approx a$). The work required per unit area to separate material to crack displacements exceeding u_0 is

$$W_{tip} = 2\int_0^{u_0} p_3(u_3)\,du_3. \tag{2}$$

An asymptotically equivalent bridged crack model possesses a critical value, K_{Ic}, for the mode I stress-intensity factor that satisfies

$$W_{tip} = \frac{K_{Ic}^2}{E'}, \tag{3}$$

where E' is an elastic constant defined in Appendix A.

The critical step in applying the cohesive crack model is evaluating the relation, $\boldsymbol{p}(\boldsymbol{u})$, from which all fracture properties can in principle be predicted.

4. Analysis of fracture data for human cortical bone

We first analyze data for human cadaveric cortical bone tested using the compact-tension $C(T)$ geometry [24]. These tests and thus all model formulations pertain to pure mode I fracture, due to the symmetry of the specimen and the material; consequently, the cohesive law reduces to the scalar relation $p_3(u_3)$. Plane-stress conditions are assumed with the crack allowed to advance along a straight front ($x_1 = a$, $x_3 = 0$).

A bilinear form is assumed for $p_3(u_3)$, as illustrated in Fig. 3. This is consistent with deductions of the spatial distribution of tractions, $p_3(x_1)$, made in [24] using destructive specimen measurements. The parameters in the bilinear form will be evaluated by fitting test data for load vs. load-point displacement from Ref. [24]. The degrees of freedom available in the bilinear form prove to be sufficient to fit these data to within the experimental noise.

For the assumed bilinear traction law, the fracture energy can be partitioned as (Fig. 3)

$$W_{total} = W_{tip} + W_{brid}, \tag{4a}$$

$$W_{tip} = 2\int_0^{u_0} p_3(u_3)\,du_3, \quad W_{brid} = 2\int_{u_0}^{u_c} p_3(u_3)\,du_3, \tag{4b}$$

The subscripts "tip" and "brid" (for wake bridging) imply that a distinction exists between mechanisms acting near the crack tip and in the further crack wake, although the present analysis cannot by itself resolve whether distinct mechanisms exist. Indeed, the traction law can be calibrated without any reference to what the underlying mechanisms giving rise to nonlinearity might be; they need not be known at all.

For a monotonically decreasing cohesive traction law, the parameter p_c is equal to the unnotched tensile strength of the material under plane-stress conditions, in the idealization of the cohesive model (e.g., [28]). Higher stresses cannot be achieved because the material will suffer strain localization on some plane, followed by progression to failure at decreasing stresses. However, the measured tensile stress of unnotched bone specimens may differ from p_c, because strength is defect sensitive.

4.1. Compact-tension test data and analysis

The compact-tension test configuration used in [24] is shown in Fig. 4a; tests from three such specimens, of slightly varying dimensions (Table 1), are analyzed here. A calibration specimen for which results prove representative of all three test specimens was defined with dimensions $w = 16\,\text{mm}$, $h = 17\,\text{mm}$; $d_1 = 4\,\text{mm}$, $d_2 = 3.8\,\text{mm}$, and loading hole diameter $= 3.6\,\text{mm}$. In the tested specimens, a pre-crack was formed by machining a notch and then creating a small notch extension with tip radius $15\,\mu\text{m}$ by polishing with a razor blade. The notch and pre-crack are similar to a natural crack with no wake bridging, so that their total length can be modeled as the initial value, c_0, of the traction-free crack length, a_0 (measured from the center-line of the loading hole). Values of c_0 varied as shown in Table 1; the value $c_0 = 3.6\,\text{mm}$ was taken for the

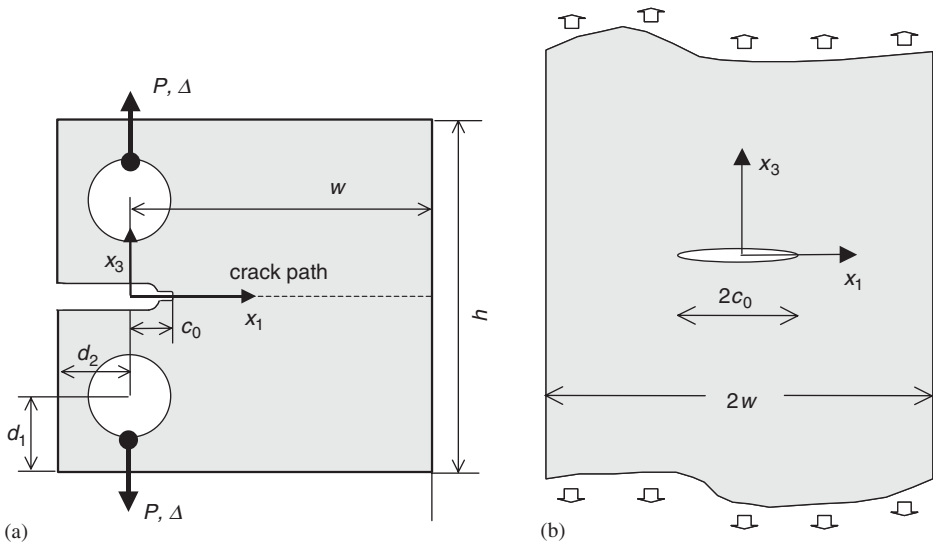

Fig. 4. Geometry of (a) the compact-tension $C(T)$ specimen and (b) a center-notch specimen.

Table 1
Dimensions (mm) of experimental test specimens

Specimens	w	h	d_1	d_2	t	c_0
1	15.7	17.0	4.0	3.8	2.5	3.6
2	16.0	15.6	3.7	3.7	2.35	3.75
3	17.0	16.8	4.1	3.8	1.9	4.1

calibration specimen. The specimen was oriented as shown in Fig. 5, so that the crack propagated along the long axis of the bone, from the proximal towards the distal end.

The load vs. load-point displacement data taken during the loading of the three specimens show an initial linear regime followed by nonlinearity (reduction of the tangent stiffness) until peak load is achieved, followed by a decline in the load (Fig. 6). The downward spikes in the post-linear curve mark instances of partial unloading to measure the residual stiffness of the specimen. The envelopes of the three sets of load–displacement data shown in Fig. 6, up to the point of unloading, were fitted to evaluate the parameters of the cohesive law.

The experiment was simulated with finite-element analysis, using the commercial ABAQUS software (version 6.4; ABAQUS, Inc., Pawtucket, RI 02860). The possibility of a cohesive zone was introduced by incorporating a set of special cohesive elements, which allow a displacement discontinuity when a critical stress is reached at any point along the potential crack path. The numerical formulation of the cohesive elements is described in Ref. [40]. The mode I cohesive traction law, $p_3(u_3)$, was assigned the piecewise linear form shown in Fig. 3, modified to include an initial linearly rising segment with a slope equal to $1000p_c/u_c$ (not shown in Fig. 3), which aids in numerical stability without altering the outcome. The loading pin was modeled as a rigid cylindrical shell coupled to the specimen by contact elements.

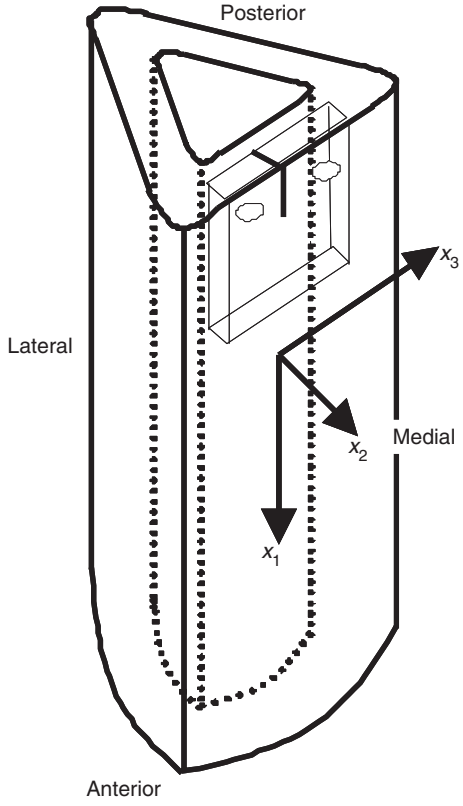

Fig. 5. Schematic illustrating the orientation of the $C(T)$ specimens in the humerus from which they were extracted.

4.2. Elasticity of the specimen

Literature data for similar bone shows values of the Young's moduli E_1 in the range 16–20 GPa and E_3 in the range 10–14 GPa [41–45]. Shear moduli, μ_{ij}, have been

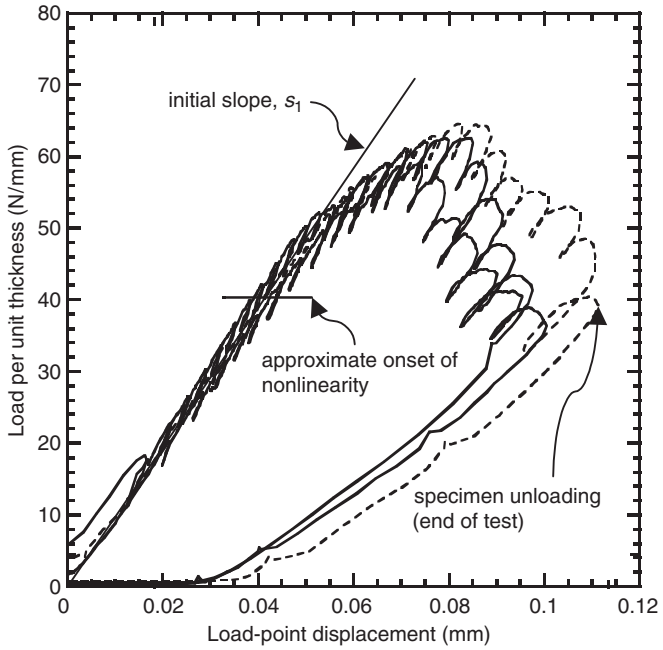

Fig. 6. Fracture data in the form of normalized load vs. load-point displacement data for cortical humeral bone from three $C(T)$ specimens [24].

measured either by ultrasound propagation or torsion tests. Ultrasound measures dynamic elasticity at very small strains, which may not be representative of static elasticity at the relatively high strains achieved in a fracture test, even where the specimen remains ostensibly linear. Torsion tests have not been applied, to the authors' knowledge, for the modulus μ_{31}, which is germane for the present compact-tension tests, presumably because shear tests are difficult to perform on specimens cut with this alignment. Reported mechanical test data for μ_{23} come from other test configurations, for whose analysis the different shear moduli are often assumed equal. With substantial variability evident in the literature, reported shear moduli range from 3 to 6 GPa (a range that covers all components). This range extends significantly lower than would be expected if the material were isotropic and Young's modulus fell in the ranges reported for E_1 and E_3. For example, taking $E = 16$ GPa and Poisson's ratio $\nu = 0.3$ in an isotropic material, one finds $\mu = 6$ GPa. Thus orthotropic elasticity is a more reasonable idealization of cortical bone for general cases than isotropic elasticity. The present data will support this view.

For the specimens to be analyzed here, no independent measurements of elasticity were made. This in fact will be a common situation, because the shape of a fracture specimen is not well suited to mechanical tests of the nine components of elasticity of an orthotropic material. Furthermore, since cortical bone is inhomogeneous over length scales of order 10 mm (the scale of features in the parent bone), elasticity measurements from different specimens cannot be assured to represent the elasticity of a given fracture specimen.

A practical resolution of this difficulty is found in the compact-tension test data themselves. Because no evidence of crack growth or damage could be seen in the experiments up to the point where the load–displacement data become nonlinear (Fig. 6), the slope, s_1, of the initial linear portion should be independent of the cohesive law (since there is no crack, only a traction-free notch and notch extension). It reflects only the elastic compliance of the specimen. For plane-stress conditions, the three components of elasticity that influence s_1 significantly are the Young's moduli, E_1 and E_3, in the x_1 direction (long axis of the bone) and x_3 direction (circumferential direction of the bone); and the shear modulus, μ_{31}, in the x_1-x_3 plane. Thus,

$$s_1 = E_1 f\left(\frac{E_3}{E_1}, \frac{\mu_{31}}{E_1}\right), \tag{5}$$

for some function f, which is dimensionless, provided that the ordinate in Fig. 6 refers to the force per unit specimen thickness. The behavior of this function is detailed in Appendix B.

For calibrating the cohesive law, Young's moduli were assigned the values $E_1 = 16$ GPa and $E_3 = 12$ GPa. The shear modulus, μ_{31}, was then determined from the measured slope, s_1, using Eq. (5), resulting in the value $\mu_{31} = 1.5$ GPa. For the test data of Fig. 6, $s_1 = 1050 \pm 50\,\mathrm{N/mm^2}$, the error representing variance from specimen to specimen.[2] The only other elastic constants that enter into the plane-stress problem are Poisson's ratios in the x_1-x_3 plane, ν_{31} and ν_{13}. The former was assigned the typical literature value, $\nu_{13} = 0.3$; the latter is then implied by the relation $\nu_{31}/E_3 = \nu_{13}/E_1$.

4.3. Calibrating the cohesive law

The problem is to evaluate the four coefficients, p_c, p_0, u_0, and u_c, of Fig. 3. This was done by a process of trial and error, minimizing the residual difference between the prediction and the data of Fig. 6.

Discussion of the fitting will refer to several key features of the load–displacement data: (i) the slope of the linear region, reproduced by proper choice of elastic constants, (ii) the stress at the onset of the first significant nonlinearity, which is marked in Fig. 6, (iii) the predicted shape of the load–displacement curve between the onset of nonlinearity and peak load, (iv) the location of the peak, in load and displacement, and (v) the slope of the curve beyond the peak.

Numerous trials showed that the onset of nonlinearity is sensitive to the contribution to the work of fracture that has been designated W_{tip} (Eq. (4), i.e., the traction law up

[2]The displacement data reported in Ref. [24] were the displacements of the actuator of the testing machine. As greater sensitivity is required for the present analysis, the same data are reported here, but with the displacements in the frame and load cell of the testing machine subtracted out. This gives a more accurate representation of the displacement of the material itself at the loading point of the specimen.

to $u_3 = u_0$, but not to the parameters p_c p_0, and u_0, which define this part of the law, separately. Fitting the onset of nonlinearity yields $W_{tip} = 0.544\,kJ/m^2$. The predicted onset of nonlinearity corresponds to the development of a cohesive zone of small, but non-zero length, along which the bridging traction diminishes from p_c to approximately p_0. The first attainment of the condition $\sigma_{33} = p_c$ at the root of the notch extension ($x_1 = c_0$), and therefore the first activation of the cohesive zone, will have occurred considerably before this point in the load history. However, this earlier event has no significant immediate effect on the load–displacement curve; only when the crack opening at the root of the notch extension begins to exceed u_0 does the curve become noticeably nonlinear. Once W_{tip} is set, changing the parameter p_c also has no significant effect on the remainder of the load–displacement curve. Therefore, p_c cannot be separately determined from the load–displacement data.[3] A prescribed value is suggested for p_c, namely $p_c = 60 \pm 10\,MPa$, consistent with literature data for the unnotched tensile strength in the circumferential direction of human Haversian bone [15,42].

The remaining parameters were varied to fit the data beyond the onset of nonlinearity. Three predictions that are optimal or near-optimal fits are shown in Fig. 7 (trials 2–4). For trials 2–4, the traction law is the same in each case up to $u_3 = u_0$, preserving $W_{tip} = 0.544\,kJ/m^2$. The fourth curve in Fig. 7 (trial 1) is the prediction found if the cohesive traction law is reduced to a simple triangle with work of fracture equal to $W_{total} = W_{tip} = 0.544\,kJ/m^2$. Since the law for trial 1 has a different shape up to $u_3 = u_0$, it must have a steeper initial slope than the laws for trials 2–4 to achieve the stated condition on the work of fracture. The parameter values for the four trials are shown in Table 2.

In the nonlinear regime immediately after the onset of nonlinearity, the curve for trial 1 rises slightly and then falls, with the ultimate load barely exceeding the load to nonlinearity. The curves for trials 2–4 at first rise in unison in the nonlinear regime and do not soften as rapidly as the curve for trial 4, because of the greater (negative) slope of the law for trial 4. Beyond a certain load, the curves for trials 2–4 show distinct behavior, rising at different rates and reaching different ultimate loads. Beyond the ultimate load, they fall with similar slopes. The ultimate load and displacement rise with W_{brid} (or W_{total}) for the three trials shown.

Many other trials were run, including trials for traction laws in which the tail ($u_3 > u_0$) was rectangular ($dp_3/du_3 = 0$) or hardening ($dp_3/du_3 > 0$). A qualitative summary of how features of the predicted load–displacement curves are sensitive to the different traction law parameters is as follows. The initial slope of the law, dp_3/du_3 for small u_3, influences the slope of the predicted curve immediately following the onset of nonlinearity, but not for long. Most of the shape of the nonlinear regime is determined by the shape of the tail to the traction law (i.e., p_3 for $u_3 > u_0$) and the corresponding contribution to the work of fracture, W_{brid}. For hardening laws, the nonlinear regime is predicted to be concave, rather than convex, in contradiction of the experiments. For rectangular laws, the gradually softening behavior of the predicted curves up to the peak load is not reproduced; the predicted curve tends to be piece-wise linear, the specimen displacement at ultimate tends to be underestimated, if the law is chosen to yield a correct prediction of the ultimate load, and the slope of the predicted curve following peak load tends to be overestimated. For bilinear softening laws, only those near to the three trials shown in Fig. 7, both in the values of p_0 and u_c (or equivalently, p_0 and W_{brid}), show a satisfactory fit to the data. Reciprocally, the ultimate load and the ultimate displacement tend to determine these tail parameters of the cohesive law.

In total four degrees of freedom are determined by the data, which, in the preceding discussion, have been represented by W_{tip}, dp_3/du_3 (for small u_3), p_0, and u_c.

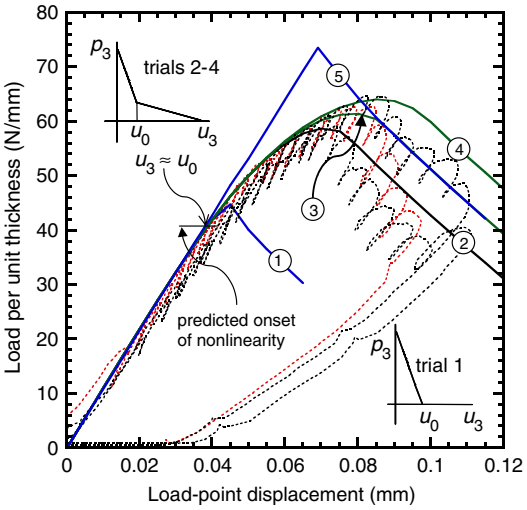

Fig. 7. Calibration of the cohesive law using the data of Fig. 6. For parameters in trials 1–5, see text.

Table 2
Parameter values of the cohesive traction law for the trials of Fig. 7

Trial	p_c (MPa)	p_0 (MPa)	u_0 (μm)	u_c (μm)	W_{tip} (kJ/m^2)	W_{brid} (kJ/m^2)
1	60	0	9.44	9.44	0.544	—
2	60	30	6.04	25.23	0.544	0.576
3	60	30	6.04	30.43	0.544	0.732
4	60	30	6.04	35.97	0.544	0.898

[3]This is hardly surprising. Since the crack tip in the model is infinitely sharp, a singularity would exist at the crack tip as long as the material remains elastic, if not for the finiteness of the numerical mesh. The maximum stress realized obviously rises as the mesh is refined; and the external load for first failure diminishes reciprocally. However, the range of the high elastic stress values is extremely limited, so that this first failure affects a very small domain and has negligible effect on the global stiffness of the specimen. This sequence of events in the model has no clear parallel in the material itself, which cannot support an elastic singularity.

These quantities can be mapped onto the set $\{p_c, u_0, p_0, u_c\}$. The deduced best-fit parameter values are close to those of Trial 3, viz., $p_0 = 30 \pm 5$ MPa, $u_0 = 6 \pm 0.5$ μm, $p_0 = 60 \pm 10$ and $u_c = 31 \pm 6$ μm, with the errors estimated from the variance among trials 2–4. (Not all of the errors can be independent, because of the constraint of satisfying the optimal value of W_{tip}.) These parameter values lead to $W_{brid} = 0.74 \pm 0.16\,kJ/m^2$, which, with the fitted value $W_{tip} = 0.54\,kJ/m^2$, yields $W_{total} = 1.28 \pm 0.16\,kJ/m^2$.

4.4. Effect of uncertainty in the elastic constants

The influence of the assumed values of the elastic constants on the deduced cohesive law was checked by varying E_1, E_3, and μ_{31} over ranges typical of the variance in literature values, always subject to the constraint of Eq. (5). Predicted load–displacement curves using the modified elastic constants but the same optimal parameter values for the cohesive traction law were almost indistinguishable from those predicted with $E_1 = 16$ GPa and $E_3 = 12$ GPa. This is an important and useful result; consistent inferences of traction laws can be made from a single test, without special efforts to measure the elasticity of the test specimen independently.

On the other hand, if isotropic elasticity were assumed for the present specimens, errors would be quite severe. First, Young's modulus would have to be reduced to a value, $E \approx 7.4$ GPa, that is well below the range of reasonable values to fit the slope, s_1. Second, the deduced traction law would be significantly different to that deduced using orthotropic elasticity.

5. Test of predictive capability

The universality of the calibrated law was tested by attempting to predict load–displacement data published by Akkus et al. [46] for nominally healthy humeral cortical bone taken from the cadavers of males aged 37–40 years. Those data were taken using a compact-tension specimen, but with different dimensions ($w = 14.2$ mm, $h = 17.0$, $c_0 = 6.78$ mm, $t = 3.16$ mm) and modified by the inclusion of side grooves along the projected crack plane. The significant difference in c_0 (at least 70% longer than for the specimens used in [24]) and the presence of side grooves, where the local thickness is reduced to 1.31 mm, resulted in a substantially different load–displacement curve, with the peak load per unit thickness (see Appendix C for definition of thickness for the grooved $C(T)$ specimen) reduced by more than 50% and the displacement at peak load 20% lower (Fig. 8). Prediction was attempted using the same elasticity and same cohesive law as established by the data of Nalla et al., with *no* alteration or iterative adjustment; only the specimen geometry was changed (see Appendix C for details of the model definition). Results are shown for each of the parameter sets of Trials 2–4 of Table 2 (Fig. 8). All three trial parameter sets fall well within experimental error up to peak load. Some variance arises following peak load, the data tending to fall faster than the predictions. The same discrepancy is visible in Fig. 6. One possible cause of this is rate-dependent softening of the cohesive tractions, which was not modeled. The agreement of the prediction with the data overall is excellent.[4]

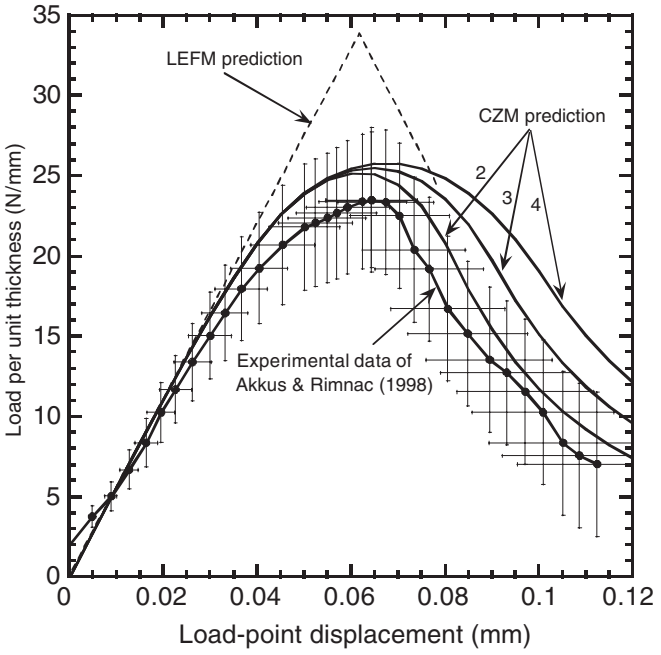

Fig. 8. Prediction of the data of Akkus et al. [46] using the cohesive law calibrated against the data of Nalla et al. [24]. The load is normalized by the quantity $\{t_g t\}^{1/2}$ (see Appendix C). LEFM prediction, using K_{Ic} evaluated from the data of Nalla et al., is also shown.

6. An internally consistent model of fracture in bone

6.1. Characteristics of the deformation field

The $C(T)$ specimen can be regarded, for building intuition into its behavior, as comprising two loaded cantilever arms, which join at the crack tip. The arms deform approximately as stubby Timoshenko beams, subject to built-in boundary conditions at the crack tip. Thus, the displacement of the loading points is a combination of bending and shear, with shear perhaps the dominant contribution, due to the stubbiness of the arms. Indeed, as detailed in Appendix B, the load-point displacement is sensitive to the choice of both the shear modulus and Young's moduli in these specimens. In other words, by virtue of its geometry, the $C(T)$ specimen can be a good test of elastic anisotropy in the tested material. This

[4]The difference in geometry between the tests of Refs. [24] and [46] leads to a large change in the peak load (≈40%), which has been predicted here using a calibration based on the average of the three tests in Fig. 6. Interestingly, the finer variations that occur within the three data sets of Fig. 6 (~9%) due the smaller geometrical variations of Table 1 can also be accounted for by using a cohesive model calibrated on just one of them, as described elsewhere [47]. The conclusions of this paper would not be affected by using this alternative calibration.

underpins the merit of using the measured elastic compliance of the specimen itself to derive the information needed about elasticity to complete the nonlinear fracture analysis.

A typical plot of the distribution of the stress component, σ_{33}, i.e., the component normal to the fracture plane, is shown in Fig. 9, for near-optimal cohesive traction law parameters. All fields are elastic, the nonlinearity of the specimen being confined in the model to the line $x_3 = 0$. A tensile field surrounds the nonlinear process zone. The bending character of the specimen is evidenced by a countering compression field at the far specimen boundary. The non-uniform curvature of the upper specimen boundary is one indication of the presence of shear deformation.

A series of snapshots of the distribution of σ_{33} along the fracture plane reveals the predicted behavior of the nonlinear damage during an experiment (Fig. 10a). The location of the crack tip (furthest extent of damage) is marked by the point where $\sigma_{33} = p_c = 60$ MPa in each case. The cohesive zone (where σ_{33} is in equilibrium with the bridging traction, p_3) can be identified as the region of approximately (but not necessarily exactly) bilinear variation of σ_{33} with x_1, where σ_{33} decreases from $\sigma_{33} = 60$ MPa to zero as x_1 decreases, i.e., as one moves further into the crack wake. The first case shown corresponds to the onset of nonlinearity marked in Fig. 7. This is the case for which the knee in the cohesive tractions (the discontinuity in slope in the bilinear shape of $\sigma_{33}(x_1)$) first appears in the cohesive zone. After the cohesive zone fully develops (between 2 and 3), it translates across the specimen with fixed length (cases 3 and 4), until the crack tip approaches the far side of the specimen, whereupon it begins to shrink (case 5). The latter effect is caused by enhanced rotation due to bending when the surviving ligament of intact material decreases; the crack must open more rapidly and the condition $u_3 = u_c$ is therefore met nearer to the crack tip [34].

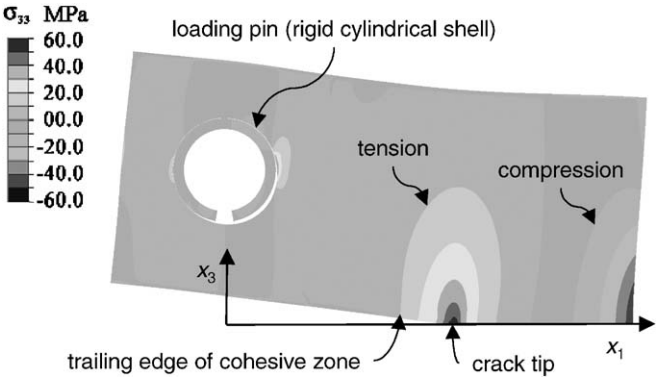

Fig. 9. Typical predicted distribution of the component of stress, σ_{33}. Only the top half of the specimen is shown.

6.2. Mesh requirements

One requirement for achieving mesh-independent predictions is that the numerical element size must be small compared to the cohesive zone [40]. More stringently, for correct prediction of the onset of nonlinearity, it must also be smaller than the length of the first linear segment in the cohesive zone, i.e., the zone length in case 1 in Fig. 9, or approximately 0.5 mm. On the other hand, since nonlinearity does not arise in the load–displacement curves until the configuration of case 1 is reached, the onset of nonlinearity is not sensitive to the maximum stress in the zone at this epoch, but to some weighted average of the stress over the zone, which extends to the point where the condition $u_3 = u_c$ is satisfied. This is consistent with the onset of nonlinearity being determined by W_{tip}, rather than p_c or u_0 separately. Furthermore, since the radius of curvature of the notch extension, 15 μm, is much smaller than the zone length at the onset of nonlinearity, no significant error is introduced by neglecting this geometrical feature in the definition of the model; similarly, there is no error by choosing a mesh that is larger than 15 μm

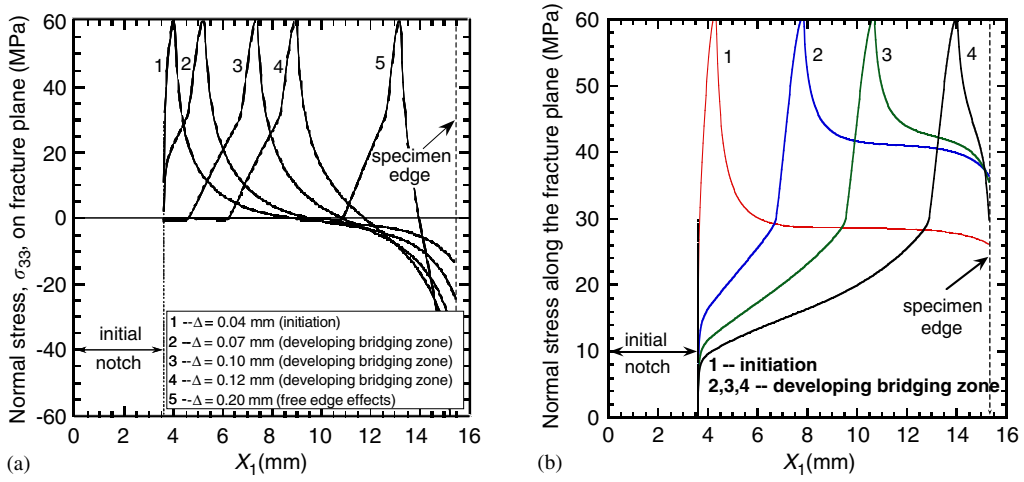

Fig. 10. Predicted distribution of the normal component of stress along the fracture plane: (a) compact-tension specimen and (b) center-notch tensile specimen.

which would be unable to predict the details of the stress concentration associated with the notch tip.

6.3. Considerations of length scales

Within an order of magnitude, the length of the cohesive zone, $\lambda_b = a - a_0$ (Fig. 2), is given by a characteristic length, l_{ch}, which can be estimated from the cohesive law [28–30,48]. For a mode I crack:

$$l_{ch} = \frac{W_{total} E'}{p_c^2}, \tag{6}$$

where E' is defined in Appendix A and takes the value $E' = 7.88\,\text{GPa}$ for the elastic constants $E_1 = 16\,\text{GPa}$, $E_3 = 12\,\text{GPa}$, and $\mu_{31} = 1.5\,\text{GPa}$ (E' is not strongly sensitive to Poisson's ratios). (See Appendix D for further remarks on the elastic constant that appears in Eq. (6).) With $p_c = 60 \pm 10\,\text{MPa}$ and $W_{total} = 1.28\,\text{kJ/m}^2$, $l_{ch} \approx 2.8\,\text{mm}$, which is in fact quite close to the calculated zone length of 3.2 mm (Fig. 9). This value of l_{ch} is also consistent with microscopic observations, which show zones of crack bridging typified by Fig. 1 in the range $\lambda_b = 5-6\,\text{mm}$.

While these results are encouraging and give important insight, the reality is that using the length of the damage zone to characterize a fracture process will always be problematic. First, the furthest progression of damage in a bone specimen may consist of microscopic or sub-microscopic (down to nano-scale) nonlinear strains, which are very difficult to detect in any fracture experiment. Because the mineralized domains of bone are generally separated by collagen or other proteins, incipient damage may consist not of brittle fracture of the mineralized constituent, but small strain localizations within the organic phase. The organic phase separates the mineralized phases, which therefore do not form a continuously connected domain; consequently, high-resolution images of bone fracture, such as Fig. 1, show no single location that can be clearly identified as the furthest progression of damage, but rather a disconnected series of fracture events. The presence of an unseen microcrack or strain localization event, beneath the observed surface or on the surface but with associated displacement discontinuity beneath the resolution of the experiment, is difficult to discount. Experimental observations should therefore be regarded as yielding a lower bound to λ_b. Second, from a modeling viewpoint, the length of the predicted damage or cohesive zone is quite sensitive to the shape of the assumed cohesive law. In the extreme, if a law is chosen in which $p_3(0) = 0$, then the cohesive-zone length in a specimen loaded in uniform remote tension will be predicted to be infinity at the first loading [29]. A fracture model using a cohesive law such as that in Fig. 3 will yield a lower bound to λ_b under variations in which $p_3(0) \to 0$ [49]. Finally, for a given traction law, both experiments and models will exhibit different zone lengths for different loading conditions and specimen geometry, as discussed below.

In spite of these sources of variance and uncertainty, the experimentally observed value of λ_b and that predicted by Eq. (6) stand firm as estimates of the process-zone length to within a factor of order unity. Strong conditions are thus implied by Eq. (6) for a fracture model to be internally consistent. In particular, only in the limit that the traction-free crack length, a_0, is much greater than l_{ch} and the damage zone does not approach other specimen boundaries, will the crack propagate under conditions that are well described by LEFM. Only under these quite restrictive conditions (Fig. 9) will fracture toughness exist as a material constant, expressed, for example, as a critical value of the strain-energy release rate, G_{Ic}. In this limit, G_{Ic} will given by [50,51]

$$G_{Ic} = W_{total} = 2\int_0^{u_c} p_3(u_3)\mathrm{d}u_3. \tag{7}$$

This limit is known in the bridged crack literature as small-scale bridging conditions.

The extent to which the bone studied here departs from LEFM conditions can be illustrated by predicting the load–displacement curve that would result if LEFM conditions are assumed (work of fracture concentrated at a point at the crack tip) and the bone is attributed a fracture toughness given by Eq. (7). This is shown in Fig. 7 by the curve labeled "5". The peak load is overestimated by 10–15% and the shape of the load–displacement data is reproduced very poorly. Another test of LEFM was made by attempting to predict the experiment of Akkus et al. with a value of K_{Ic} calibrated using the data of Nalla et al. The peak load is overestimated by 40%. Thus LEFM is a poor model for this material.

6.4. Association of mechanisms with characteristics of the traction law

The inference of the traction law from load–displacement data is a fracture analysis, not a material model, and neither relies on knowledge of nor gives any direct information about the physical mechanisms involved in the damage (cohesive) zone or the fracture process. In particular, the inferred traction law offers no information on whether distinct mechanisms are associated with the crack tip and the crack wake. The choice of a bilinear traction law was arbitrary, as was its division into what have been termed, for convenient discussion, crack tip and bridging contributions, W_{tip} and W_{brid}, to the work of fracture. A law consisting of a monotonically decreasing function, following the general shape of the bilinear law of Fig. 3, but without a discontinuity of slope, would probably fit the load–displacement data just as well; there is not enough information in load–displacement data to resolve such a fine distinction.[5]

[5]For such a smooth law, one would still expect, based on the analysis here, to determine four degrees of freedom, e.g., p_c, the initial slope $\mathrm{d}p_3/\mathrm{d}u_3$ for small u_3, the curvature of the law, and u_c.

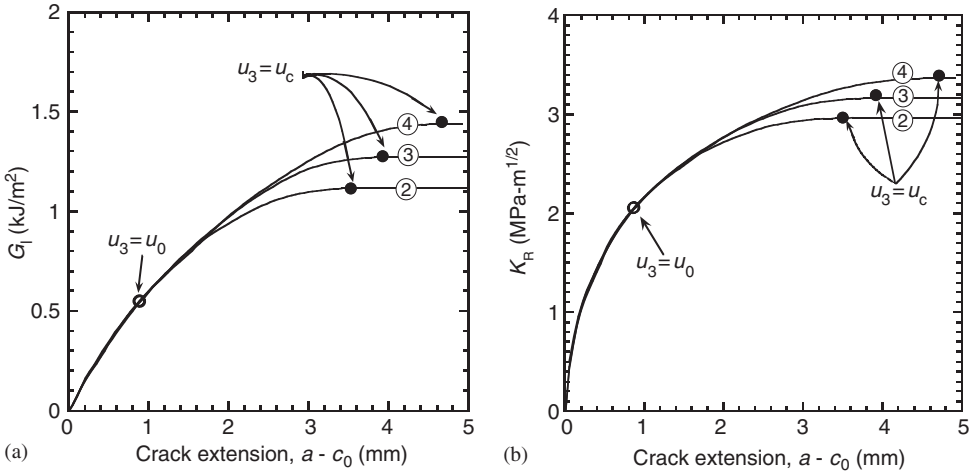

Fig. 11. R-curve predictions for the parameters of trials 2–4 of (a) the incremental work of fracture (per unit crack extension and crack width) and (b) the apparent mode I fracture toughness as a function of crack length, measured to furthest extent of damage (compact-tension specimen). The conditions $u_3 = u_0$ (onset of nonlinearity in the load vs. load-point displacement curve) and $u_3 = u_c$ (fully developed cohesive zone) are marked.

Information about fracture mechanisms must come from other sources. Observations of mechanisms point to bridging, principally by intact ligaments of mineralized bone and to a lesser extent (and on a smaller scale) by fibrils of collagen (Fig. 1) [4]. Assuming that these mechanisms co-exist, the cohesive traction law may be interpreted as representing their net effect, operative wherever the material is nonlinear.

The fact that nonlinearity in the load–displacement data occurs at a large, non-zero value of the load can be attributed to the necessity (i) of attaining a critical value of the local stress before material is damaged, and (ii) that this should occur over a sufficiently large gauge for the fracture test to be measurably influenced. This product of stress and gauge length is linked qualitatively to what has been called W_{tip} in this work. Progression from this first measurable damage, with crack displacements $u_3 < u_0$, to a fully developed cohesive zone can occur, as the cohesive model has demonstrated, with no disruption or discontinuity in the stress fields associated with the evolving cohesive zone. In other words, the same mechanisms that give rise to first nonlinearity can also, as they evolve and support decreasing loads, account for the softening process along the whole cohesive zone, i.e., the whole crack wake. Such a view of common mechanisms for all crack displacements has some appeal in a heterogeneous composite such as bone, for the reasons discussed above.

6.5. Prediction of the R-curve

With the cohesive law established, predictions of all measurable aspects of a fracture experiment are available. In particular, the conditions under which LEFM is a satisfactory representation of fracture data can be quantified.

As the crack progresses, the work expended in the fracture process can be deduced from the bridging tractions, which represent the nonlinear mechanics of the process zone. The work expended in fracture, G_I, per unit specimen width and unit increment in crack length, is given by [52,53]

$$G_I(a) = 2\int_0^{u_{\max}(a)} p_3(u_3)\mathrm{d}u_3, \tag{8}$$

where $u_{\max}(a)$ is the maximum crack opening attained at crack length a, defined as the furthest calculated advance of the damage zone (condition $\sigma_3 = p_c$). Given G_I, the apparent critical mode I stress-intensity factor, K_R, at a particular crack length follows from

$$K_R(a) = \sqrt{G_I(a)E'}, \tag{9}$$

where E' is an elastic constant, defined for an orthotropic material in Appendix A. The function $K_R(a)$ is the R-curve. The functions $G_I(a)$ and $K_R(a)$ are plotted for the $C(T)$ specimen in Fig. 11, for the parameter sets of trials 2–4 (Table 2). The onset of nonlinearity in the load vs. load-point displacement curve occurs near the condition $u_3 = u_0$, while the attainment of a fully developed cohesive zone occurs exactly (within the domain of the model) at the attainment of the condition $u_3 = u_c$. Upon the satisfaction of the latter condition, the curves for either G_I or K_R become independent of crack length and in particular $K_R \to K_{Ic}$, the critical stress-intensity factor (i.e., fracture toughness) of LEFM.

The onset of nonlinearity also corresponds approximately to the conditions reported previously as crack initiation [24]; the concomitant value $K_R = 2.1\,\text{MPa} - \text{m}^{1/2}$ corresponds to that reported for the initiation toughness, K_{init}. While the data of Ref. [24] do not clearly show a plateau for the crack lengths that were attained, the predicted plateau value $K_R = 3.0$–$3.4\,\text{MPa-m}^{1/2}$ is similar to the maximum K_R in the data. Attaining a steady-state condition in $K_R(a)$ is a necessary condition for LEFM to be valid. The present

predictions show that the required crack growth in the compact-tension configuration is ~5 mm.

A discrepancy may arise between the model predictions of both K_{init} and K_{Ic} and those reported in prior analyses of experiments, including Ref. [24], because in the present work, the elastic constant E' is evaluated for orthotropic elasticity. This results in a value for E' that is approximately 50% of the value that would follow if isotropic elasticity had been assumed, with a consequent error in K, when evaluated from a measurement of the work of fracture (Eq. (9)), of approximately 30%. An error of similar magnitude to this could arise in prior reports of K_{Ic} for humeral cortical bone wherever elastic anisotropy has been overlooked. The actual error will depend on the elasticity of the bone specimen and the test configuration.

6.6. Similarity to nonlinear fracture models of concrete

Many of the earliest applications of cohesive zone models to fracture problems were for concrete, beginning with the seminal paper of Hillerborg et al. [30]. That the fracture of concrete should have inspired a nonlinear treatment is attributable to the fact that fracture process zones in concrete are remarkably long—typically substantial fractions of 1 m. The common perception of concrete as a brittle material is a little misleading in this aspect. With such long process zones, size effects in strength that cannot be described by LEFM are inevitable (e.g., [30,54,55]). The fracture process zone in concrete shows some characteristics that are quite similar to those seen in cortical bone, especially the presence of systems of mother-daughter cracks, with surviving ligaments of material providing bridging across the damage zone (the physical source of the cohesive tractions). Furthermore, the cohesive law that applies to concrete is, like that determined here for cortical bone, a softening law (traction decreasing with increasing crack displacement), which is, furthermore, often represented successfully as a bilinear function (e.g., [56]).

7. Effect of specimen configuration on predicted characteristics

Model calculations using the optimal cohesive law allow the effect of choosing specimen configurations that are different from those used in [24,46] on deduced bone properties to be quantified. To illustrate specimen dependence, predictions are compared for the compact-tension specimen used in the experiments of Ref. [24] and a plate with a centered notch under uniform remote tension (Fig. 4b). The center-notch specimen is distinguished qualitatively from the compact-tension specimen by greatly reduced bending and shear in the displacement fields and much lower crack-tip constraint. It consists of a tensile plate with width $2w = 32$ mm (twice that of the active section of the $C(T)$ specimen) and an initial traction-free notch of length $2c_0 = 7.2$ mm (again twice that of the notch plus notch extension in the $C(T)$ specimen). Boundary conditions are imposed that generate a state of uniform remote tension in the direction normal to the plane of the notch.

Substantial differences arise in the predicted distribution of stresses along the fracture plane during crack growth for the two specimens (Fig. 10). There is no compressive zone in the tensile specimen, and the cohesive zone does not reach a fully developed condition ($\sigma_{33} = 0$ in the crack wake), even when the crack tip approaches the specimen boundary (Fig. 10b). In the fourth epoch illustrated in Fig. 10b, the cohesive zone (extending from the peak stress back to the notch root) has almost spanned the entire net section of the tensile specimen, exceeding 11 mm. Thus, for this specimen configuration and the same material constitutive properties (elastic anisotropy and cohesive law) as those deduced from the compact-tension experiments, the steady-state condition required for LEFM to be approached is never attained. This means that a compact-tension test, analyzed by LEFM, *could not account* for the fracture behavior of the tensile specimen.

Consistent differences between the two specimens arise in the predicted R-curves. The apparent mode I fracture toughness, K_R, rises much more slowly with crack extension, a–c_0, in the case of the tensile center-notch specimen and does not reach the asymptotic steady-state value (Fig. 12). Furthermore, the slope of the R-curve, which controls the stability of crack growth for different notch sizes, is test-configuration dependent. The slope determined from one test may give misleading predictions of crack stability in general.

The load–displacement curves for the two specimens are also quite different (Fig. 13). Even when the load per unit thickness is normalized by the specimen width, the loads for the $C(T)$ specimen are an order of magnitude lower, a result of the stress concentration at the notch root due to bending and shear. Interestingly, the predicted curve for the center-notch tension specimen shows a relatively small increase of load beyond the first visible nonlinearity and a rapid drop in load beyond ultimate. These characteristics might be mistaken for a brittle fracture process (fracture process confined to a small volume near the notch root, prior to unstable crack propagation), but in fact Fig. 10b shows this is far from the case. It is, to the contrary, the nature of this specimen configuration that the damage zone spans the entire section of the specimen (excluding the notch) before ultimate and the brittle appearance of the load–displacement curve derives from the fact that the bridging material in the cohesive zone fails almost simultaneously across the whole specimen. Because of these mechanics, load–displacement data from the center-notch tension specimen would be less suited to the deduction of the traction law than are the compact-tension data.

As for the $C(T)$ specimen, LEFM would make a poor prediction of the load–displacement data for the center-notch tension test. The LEFM prediction, made with a fracture toughness equal to the work required to rupture the cohesive elements (Eq. (7)) all concentrated at the crack

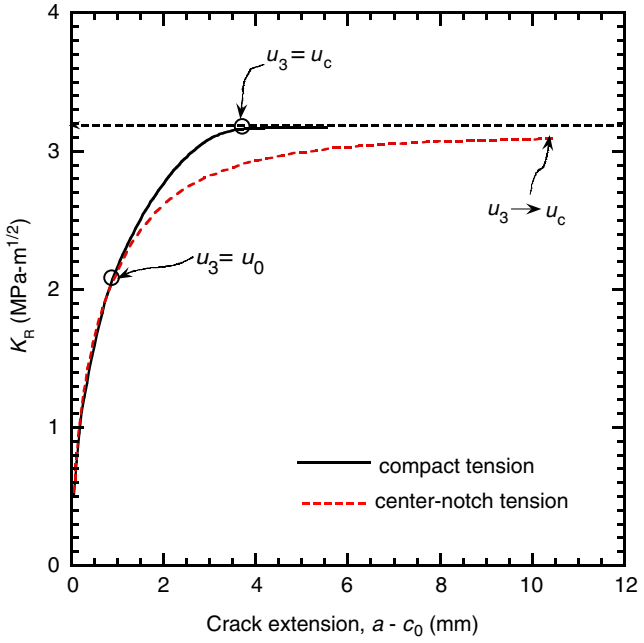

Fig. 12. Predictions of the apparent mode I fracture toughness as a function of crack length, measured to furthest extent of damage (compact-tension and tensile center-notch specimens).

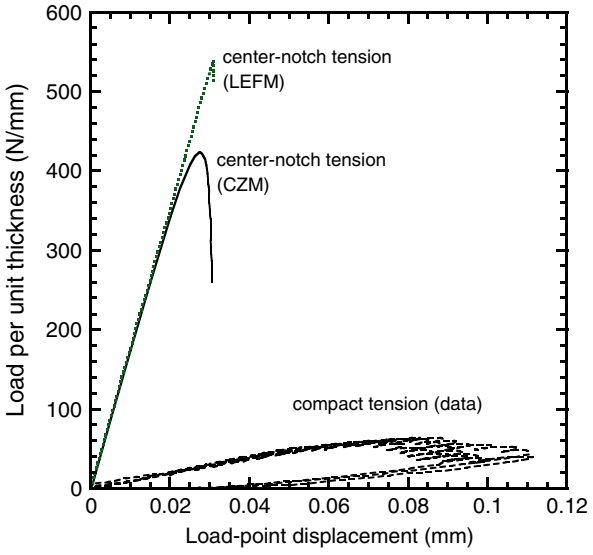

Fig. 13. Comparison of load–displacement curves for compact-tension and center-notch tension specimens. The curves for the compact-tension test are the experimental data; the curves for center-notch tension are predictions using the cohesive zone model. For the calculation marked LEFM, the work in the cohesive law was all concentrated at a point at the crack tip.

tip, is also shown in Fig. 13. The peak load is overestimated by approximately 23%. Comparison with Fig. 7 shows that the error incurred in the predicted peak load using LEFM is different for different test specimens. Therefore, no consistent correcting calibration for LEFM can be defined.

8. Implications for understanding bone fracture

8.1. Proposed procedure for characterizing fracture properties

Because of its more complete accounting of fracture data, the cohesive law may be a preferred material property for characterizing the fracture resistance of cortical bone. The question arises of what is the best experiment for its determination. While much further experience in data reduction must be accumulated before an authoritative answer can be reached, the first analyses described in this paper already suggest the outcome.

First, the load vs. load-point curve taken alone contains sufficient information to determine the traction law with a degree of resolution of detail that is sufficient for predicting fracture behavior. These curves are readily available from standard test procedures. The more difficult experiments of measuring crack profiles or mapping the spatial distribution of damage can certainly reveal additional information of clinical importance, but may not significantly improve the prediction of macroscopic features of fracture behavior. Such data would be relevant to models of local deformation events, rather than macroscopic cracking.

On the question of what test configuration should be preferred for acquiring load–displacement data for mode I fracture, the compact-tension test offers the following advantages. (1) Because it involves both bending and shear deformation, it provides, through the slope of the initial linear response, good information on the degree of elastic anisotropy of the material. Getting this information from the same specimen as that yielding fracture information has much merit, in view of the spatial inhomogeneity of bone. (2) Because of the presence of a compressive zone ahead of the growing crack, the process zone is relatively limited in extent, so that even in a specimen only 15–20 mm in total width, a steady-state zone is attained. Information about the complete traction law is therefore contained in the test. In contrast, a uniform tension test in a specimen of doubled width never achieves the steady state, and a portion of the traction law at high crack-opening displacements is not sensed. (3) The load vs. load-point displacement data show significantly more nonlinearity for the $C(T)$ specimen than is predicted for a uniform tension specimen, which is likely to translate to better resolution of the traction law.

As has been remarked, both experimental observations and model predictions leave the length of the process zone inexactly determined. A longer zone than observed or predicted can be present if the most advanced damage gives rise to very small net displacements. In a heterogeneous material such as bone, vanishingly small displacements in the collagen phase, in advance of those that are easily detected, are in fact quite likely. However, such an uncertainty in the total length of the damage zone has little effect on the outcome of a fracture experiment, either in the load–displacement data, the inferred traction law, or,

when a cohesive model is used for analysis, the inferred work of fracture.

8.2. Possible significance of the cohesive law in clinical studies

The value taken by the characteristic length, l_{ch}, along with the zone lengths and other fracture characteristics predicted for the cases analyzed here, have fundamental implications for assessing clinical fractures. The zone length varies with loading configuration, ranging from 3 mm (predicted) or 5 mm (experimental observation) for the compact-tension test to >10 mm for the center-notched tension test; all of which values are consistent with the order of magnitude pointer, $l_{ch} \approx 3$ mm. While detailed analysis of fracture for the real geometry of a complete bone is beyond the scope of this paper, one would expect that, of the two cases analyzed here, that of the center-notched tension test may be the more representative of the cohesive-zone behavior in, for example, a transverse femoral fracture. The degree of bending and shear deformation in a naturally occurring bending fracture of a long bone will be much less than in the $C(T)$ specimen. Bending effects in a femur, of typical diameter 20 mm, for example, will only be pronounced when the crack length is 10 mm or so; up until then, the damage zone develops in a predominantly tensile field and the zone length is likely to be closer to the higher length predicted for uniform remote tension. Therefore, small-scale bridging conditions *are unlikely to be achieved* when a crack propagates through cortical bone normal to the long axis in any human bone. The LEFM parameter, K_{Ic}, can at best be an approximate method of characterizing fracture resistance.

Neither will a single critical stress, such as the parameter p_c evaluated here (Fig. 3), be an adequate predictor of fracture. While p_c is correlated here with the onset of nonlinearity in the load vs. load-point displacement curve (or more generally, the far-field stress–strain relationship), it cannot also account for the measured ultimate load. The substantial increase of load beyond the onset of nonlinearity will only be accounted for by including the wake tractions in a fracture model, and the account will only be accurate if the distribution of tractions along the crack wake is modeled correctly.

The cohesive traction law of Fig. 3, hypothesized for analyzing the present mode I problem, provides four degrees of freedom in place of the single parameter, G_{Ic} or K_{Ic}, of LEFM. While four degrees of freedom suffice in the present case, a cohesive law for another material could possibly contain more numerous degrees of freedom. Indeed, the cohesive model formulation provides a convenient route to obtaining all the information about material behavior that can have an influence on a fracture experiment. The extent to which the shape of the cohesive law can be determined from fracture data is limited exactly by the sensitivity of the experiment to changes in the material; if the fitting procedure cannot resolve further details in the traction law, then those further details of material behavior do not matter to the fracture observables. Qualitative assessment of the present fitting exercise and prior experience with engineering materials that have similar fracture characteristics [57,58] suggest that the four degrees of freedom used here may be close to the limit of the information content of static fracture experiments on bone.

The four degrees of freedom of Fig. 3 provide much deeper insight into the nonlinear material behavior that underlies fracture than the single measure, K_{Ic} or G_{Ic}, of LEFM. For example, the stress, p_c, which is evaluated from the first onset of nonlinearity in the fracture data, may represent tensile material failure under general conditions, i.e., in the absence of a single dominant crack. Further, the critical displacement, u_c, indicates the maximum supportable displacement discontinuity, which is a measure of the material's ductility. If a measurement is available from other observations of the maximum width, w_m, of the zone of damage ($w_m = \max\{w_b(x_1)\}$, Fig. 2), then a critical strain,

$$\varepsilon_{33}^{(c)} = u_c / w_m, \tag{10}$$

can be inferred for the loss of all load-bearing capacity in the material, which might be representative of the material behavior in more general conditions. From Fig. 1 and similar images, a rough estimate is that $w_m \approx 1$ mm; together with $u_c = 35\,\mu$m, this suggests $\varepsilon_{33}^{(c)} \approx 0.03$ for the present bone specimen. Residual (small) load-bearing capacity persists to quite large local strains.

In conjunction with more detailed models of the micromechanics of nonlinear crack damage zones, the characteristics of the cohesive law, such as p_c and u_c (or the related quantity $\varepsilon_{33}^{(c)}$), are much more direct measures of the underlying damage mechanisms in the bone than is the LEFM parameter, G_{Ic} or K_{Ic}. Therefore, correlating the cohesive traction law with the use of drug therapies for bone, for example, may prove a useful way of linking therapies to desired bone performance.

9. Concluding remarks

A cohesive fracture model has been formulated and applied to data for human femoral cortical bone. The central constitutive property in the model is the relation, $\boldsymbol{p}(\boldsymbol{u})$, between the tractions supplied by nonlinear (failing) material across the fracture plane and the displacement discontinuity across the same plane. The relation $\boldsymbol{p}(\boldsymbol{u})$ is hypothesized to be a material property for a given source of bone with given age and condition. This hypothesis was tested successfully by using a relation $p_3(u_3)$, the component of $\boldsymbol{p}(\boldsymbol{u})$ pertinent to mode I fracture, calibrated against data from one laboratory to predict test results taken in a different laboratory for a different source of nominally similar bone tested in a specimen of different shape and size. When the same challenge problem was attempted using LEFM, the predicted strength was too high by

approximately 40%. That LEFM can generate an error of such magnitude in analyzing two sets of data from specimens with size variations typical of common practice raises the question of whether much of the variance in fracture resistance reported previously in the literature might arise from inadequate fracture analysis.

The onset of significant nonlinearity in the experimental load–displacement curves has been shown to be associated with the development of a cohesive zone of length ~0.5 mm over which tractions of 30–60 MPa exist, the upper value of stress being the conjectured critical value of the local stress for damage initiation. Further development of the cohesive zone occurs before and after the attainment of peak load, to a predicted total length of 3 mm. Considerable variation of the cohesive-zone length might be expected with the age and condition of the bone, shorter zones being associated with more brittle fracture, e.g., for aged or diseased bone.

Further simulations using the empirically determined relation, $p_3(u_3)$, show that strong variations can occur in fracture characteristics, when different test configurations are chosen. In a center-notch tension specimen, much more extensive cohesive zones arise, of length exceeding 10 mm. Consistently, the evolution of the apparent fracture toughness with crack length is different to that for the compact-tension test.

For LEFM to be accurate, the specimen and crack length must both exceed the process-zone length, which is indicated to an order of magnitude by the characteristic length, l_{ch}. For human cortical bone, this condition is unlikely to be met in any transverse fracture (normal to the long axis of the bone). Therefore, the fracture toughness, K_{Ic} or G_{Ic}, deduced from experiments using LEFM analysis cannot be expected to be a material constant, but will depend on the geometry and crack configuration.

The traction law, $\boldsymbol{p}(\boldsymbol{u})$, offers an internally consistent approach to accounting for all macroscopic features of fracture. It includes, in the limit of long cracks (often longer than can be sustained in a bone), the fracture toughness, K_{Ic}, represented by LEFM; it also enables prediction of the initiation and propagation of fracture when the apparent toughness is not constant and can predict the effects of specimen shape and loading configuration. Furthermore, because it describes the spatial distribution of stress over the nonlinear process zone associated with fracture, the traction law relates much more directly than does K_{Ic} to the underlying material processes. Therefore, it may prove useful in establishing clinical correlations to assess, for example, the efficacy of drug therapies that seek to improve bone quality.

The initial linear behavior of the fracture specimens analyzed here also implies that humeral cortical bone is strongly anisotropic in the elastic regime. The shear modulus in the plane of the test, i.e., the medial plane of the bone, is less than half that expected for an isotropic material (or a material that possesses a plane of transverse isotropy normal to the long axis of the bone). If Young's moduli are assigned the plausible values $E_1 = 16$ GPa and $E_2 = 12$ GPa, then the shear modulus is $\mu_{31} = 1.5$GPa. The test data analyzed from two laboratories are closely consistent on this point. Since this particular component of shear is difficult to measure independently, a procedure is suggested in which the load–displacement fracture data themselves are used to evaluate a constraint on the components of elasticity needed to analyze the fracture data. Only if the elastic constants satisfy this constraint can accuracy be anticipated in the subsequent fracture analysis: strong anisotropy has a substantial effect on the relation, in the long-crack limit where LEFM is valid, between the work of fracture and the critical stress-intensity factor. The latter may have been miscalculated in prior literature, if the material anisotropy was mis-represented.

Acknowledgements

QDY received partial support from a Rockwell Scientific seedling project. RKN was supported by the National Institutes of Health under Grant No. 5R01 DE015633 and ROR by the Director, Office of Science, Office of Basic Energy Science, Division of Materials Sciences and Engineering, Department of Energy under No. DE-AC02-05CH11231.

Appendix A. Relation between K and G for an orthotropic material

The elastic constant E' that appears in Eq. (3) is given for an orthotropic material in which a crack in plane-stress conditions propagates in the x_1 direction along the plane $x_3 = 0$ by [59,60]

$$\frac{1}{E'} = \sqrt{\frac{b_{11}b_{33}}{2}}\sqrt{\left(\frac{b_{33}}{b_{11}}\right)^{1/2} + \frac{2b_{31}+b_{55}}{2b_{11}}}, \tag{A.1}$$

where the b_{ij} are Voigt elastic constants defined by

$$\varepsilon_i = \sum_{j=1}^{6} b_{ij}\sigma_j, \tag{A.2}$$

with $\varepsilon_1 \equiv \varepsilon_{11}$, … , $\varepsilon_6 \equiv \varepsilon_{12}$; $\sigma_1 \equiv \sigma_{11}$, … , $\sigma_6 \equiv \sigma_{12}$. In plane strain, Eq. (A.1) holds with b_{11} replaced by b_{11}–b_{12}/b_{22}, b_{33} by b_{33}–b_{23}/b_{22}, and b_{31} by b_{31}–$b_{23}b_{12}/b_{22}$.[6] For a specially orthotropic specimen (axes of orthotropy aligned with the axes of symmetry of the specimen), the Voigt elastic constants are related to the engineering elastic constants by (e.g., [61,62])

$$\begin{aligned} &b_{11} = 1/E_1, \quad b_{12} = -\nu_{12}/E_1, \quad b_{66} = 1/\mu_{12}, \\ &b_{22} = 1/E_2, \quad b_{23} = -\nu_{23}/E_2, \quad b_{55} = 1/\mu_{31}, \\ &b_{33} = 1/E_3, \quad b_{31} = -\nu_{31}/E_3, \quad b_{44} = 1/\mu_{23}, \end{aligned} \tag{A.3}$$

where E_i is Young's modulus in the x_i direction, ν_{ij} is one of Poisson's ratios, and μ_{ij} is an engineering shear modulus.

[6] While the notation of [60] is more convenient to the current work than that of the original work of [59], the reader should be wary of a typographical error in [60], corrected above.

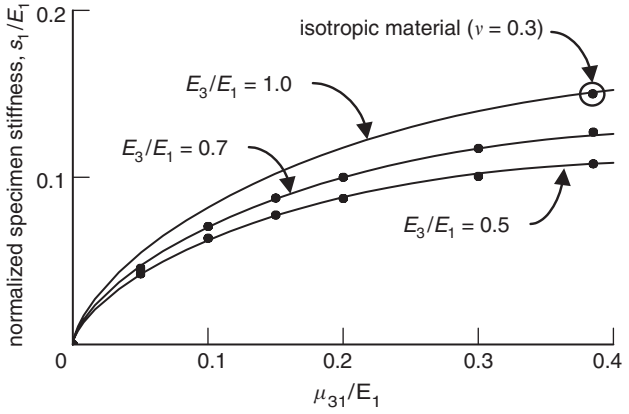

Fig. B.1. Variation of the predicted slope, s_1, with assumed elastic constants. Points show finite-element calculations and curves show the engineering approximation of Eq. (B.1).

For the alignment of the specimen in Fig. 4a, the engineering constants involved in E' are E_1, E_3, μ_{31}, and ν_{31}.

Appendix B. Elastic response of the uncracked compact-tension specimen

Numerical results for the initial linear slope of the load–displacement curve for a compact-tension specimen with the dimensions of Fig. 4a, i.e., the response prior to initiation of a crack from the notch root, are shown in Fig. B.1. The initial slope is presented as the function, f, of Eq. (5), which is the slope normalized by the modulus, E_1. An engineering approximation to the computed data is

$$f = \left(\frac{\mu_{31}}{E_1}\right)^{0.64}\left(0.2105 - 0.2337\frac{\mu_{31}}{E_1} + 0.1758\frac{E_3}{E_1} - 0.0481\frac{\mu_{31}}{E_1}\frac{E_3}{E_1}\right),$$

in the regime $0<\mu_{31}/E_1<0.4$ and $0.5<E_3/E_1<1$, provided s_1 and E_1 have the same units.

Appendix C. Representation of the side-grooved $C(T)$ specimen

For a specimen in which LEFM prevails,

$$K_{\mathrm{Ic}} = \frac{P_{\max}}{t} f(a, w), \tag{C.1}$$

for some function f of the crack length and the specimen width. From Eq. (3),

$$G_{\mathrm{Ic}} t = \frac{P_{\max}^2}{E' t} f^2(a, w). \tag{C.2}$$

For a side-grooved specimen with groove section thickness t_g, the energy dissipation per unit crack extension must be $G_{\mathrm{Ic}} t_g$, which leads in combination with Eqs. (C.1) and (C.2) to

$$K_{\mathrm{Ic}} = \frac{P_{\max}}{\sqrt{t \cdot t_g}} f(a, w). \tag{C.3}$$

Even though the tests studied here do not accord with LEFM, Eq. (C.3) recommends using the geometrical mean of the specimen thickness, t, and grooved section thickness, t_g when making qualitative comparisons of the side-grooved and the ungrooved $C(T)$ data. The data from Ref. [46] have accordingly been normalized by this thickness measure (Fig. 8).

In the numerical simulations of the side-grooved $C(T)$ specimen, the grooved section is not represented geometrically in full detail. The simulations were formulated in plane stress, with a nominal thickness associated with each element in the model (a feature allowed in ABAQUS—the thickness appears in the equations of nodal force balance expressly to permit thickness variations while retaining the simplicity of plane-stress conditions). The side-grooved section was represented as a set of plane-stress elements of reduced thickness equal to the minimum thickness of the groove, t_g. Thus, the traction force per unit crack length due to the cohesive mechanism, $p_3 t_g$, has the correct magnitude for balancing with the other stresses in the system. This simplified treatment of the side-groove geometry is a good approximation, because the elastic deformation within the grooved region (which would depend on the geometrical details of the groove) is a negligible contribution to the total displacement fields; the dominant contribution to the displacement fields from the vicinity of the crack plane arises from the displacement discontinuity, u_3, which remains accurately calculated.

Appendix D. Dependence of characteristic length, l_{ch}, on elasticity

In an infinite body that contains a bridged crack and is loaded in plane conditions, an application of Castigliano's theorem allows the crack displacement to be derived in terms of weight functions (e.g., [63]). The weight functions define the crack-tip stress-intensity factor caused by a point force acting at some distance from the crack tip. To a good approximation, the weight functions are independent of the elasticity of the material, including the degree of anisotropy, provided symmetry about the crack plane is not violated (this condition requires, for example, that an orthotropic material be specially orthotropic, i.e., that the crack plane is a plane of orthotropy) [64]. The derivation also involves the relation between the crack-tip stress-intensity factor and the energy release rate, within which an elastic constant appears (see [63] for details). For an orthotropic body, this is the elastic constant, E', defined in Appendix A. This is the only elastic constant that appears in the expression for the crack opening profile; under changes of elasticity, the cohesive zone length must, therefore, scale with E'.

For a crack in an infinite body that is loaded in shear, the weight functions remain identical in form to those for mode I (e.g., [65]) and the elastic constant that appears in the relation between the crack-tip stress-intensity factor and the energy release rate is

$$\frac{1}{E'} = \sqrt{b_{11}/2}\sqrt{(b_{11}b_{33})^{1/2} + (b_{31} + b_{55}/2)} \quad \text{(mode II)}. \tag{D.1}$$

The cohesive zone length will scale with this constant, which is essentially the same as that in Appendix A, with indices permuted.

In a slender body, a different elastic constant appears. For example, in a thin plate or beam containing a mid-plane crack propagating in the x_1 direction and loaded in mode II (applied shear, e.g., an end-notch flexure specimen), the elastic constant that appears in results for the cohesive zone length is the reduced Young's modulus:

$$\bar{E} = \frac{E_1}{1 - v_{13}v_{31}}, \tag{D.2}$$

where x_3 is the through-thickness direction and v_{ij} are Poisson's ratios [49].

References

[1] Hui SL, Slemenda CW, Johnston CC. Age and bone mass as predictors of fracture in a prospective study. J Clin Invest 1988;81(6):1804–9.

[2] Jennings AG, de Boer P. Should we operate on nonagenarians with hip fractures? Injury 1999;30(3):169–72.

[3] Schaffler MB, Choi K, Milgrom C. Aging and matrix microdamage accumulation in human compact bone. Bone 1995;17:521–5.

[4] Nalla RK, Kruzic JJ, Kinney JH, Ritchie RO. Effect of aging on the toughness of human cortical bone: evaluation by *R*-curves. Bone 2004;35(6):1240–6.

[5] Burstein A, Reilly D, Martens M. Aging of bone tissue mechanical properties. J Bone Joint Surg 1976;58A:82–6.

[6] Currey JD. Changes in impact energy absorption with age. J Biomech 1979;12:459–69.

[7] Bonfield W, Behiri JC, Charalamides C. Orientation and age-related dependence of the fracture toughness of cortical bone. In: Biomechanics: current interdisiplinary research. Dordrecht: Martinum Nijhoff Publishers; 1985.

[8] Wang XD, Masilamani NS, Mabrey JD, Alder ME, Agrawal CM. Changes in the fracture toughness of bone may not be reflected in its mineral density, porosity, and tensile properties. Bone 1998;23(1):67–72.

[9] Zioupos P, Currey JD. Changes in the stiffness, strength, and toughness of human cortical bone with age. Bone 1998;22:57–66.

[10] Phelps JB, Hubbard GB, Wang X, Agrawal CM. Microstructural heterogeneity and the fracture toughness of bone. J Biomed Mater Res 2000;51:735–41.

[11] Yeni YN, Norman TL. Fracture toughness of human femoral neck: effect of microstructure, composition, and age. Bone 2000;26(5):499–504.

[12] Rho J-Y, Kuhn-Spearing L, Zioupos P. Mechanical properties and the hierarchical structure of bone. Med Eng Phys 1998;20:92–102.

[13] An YH. Mechanical properties of bone. In: Mechanical testing of bone and the bone–implant interface. Boca Raton, FL: CRC Press; 2000. p. 41–63.

[14] Weiner S, Wagner HD. The material bone: structure–mechanical function relations. Annu Rev Mater Sci 1998;28:271–98.

[15] Currey JD. 'Osteons' in biomechanical literature. J Biomech 1982;15:717.

[16] Brown CU, Norman TL. Fracture toughness of human cortical bone from the proximal femur. Adv Bioeng 1995;31:121–2.

[17] Feng Z, Rho J, Han S, Ziv I. Orientation and loading condition dependence of fracture toughness in cortical bone. Mater Sci Eng C 2000;C11:41–6.

[18] Norman TL, Nivargikar SV, Burr DB. Resistance to crack growth in human cortical bone is greater in shear than in tension. J Biomech 1996;29(8):1023–31.

[19] Yeni YN, Brown CU, Wang Z, Norman TL. The influence of bone morphology on fracture toughness of the human femur and tibia. Bone 1997;21(5):453–9.

[20] Vashishth D, Tanner KE, Bonfield W. Contribution, development and morphology of microcracking in cortical bone during crack propagation. J Biomech 2000;33:1169–74.

[21] Nalla RK, Kinney JH, Ritchie RO. Mechanistic fracture criteria for the failure of human cortical bone. Nat Mater 2003;2:164–8.

[22] Behiri JC, Bonfield W. Orientation dependence of the fracture mechanics of cortical bone. J Biomech 1989;22(8/9):863–72.

[23] Malik CL, Stover SM, Martin RB, Gibeling JC. Equine cortical bone exhibits rising *R*-curve fracture mechanics. J Biomech 2003;36:191–8.

[24] Nalla RK, Kruzic JJ, Kinney JH, Ritchie RO. Mechanistic aspects of fracture and *R*-curve behavior in human cortical bone. Biomaterials 2005;26(2):217–31.

[25] Vashishth D, Behiri JC, Bonfield W. Crack growth resistance in cortical bone: concept of microcrack toughening. J Biomech 1997;30(3):763–9.

[26] Ritchie RO. Mechanisms of fatigue crack propagation in metals, ceramics and composites: role of crack-tip shielding. Mater Sci Eng 1988;103:15–28.

[27] Nalla RK, Kruzic JJ, Ritchie RO. On the origin of the toughness of mineralized tissue: microcracking or crack bridging? Bone 2004;34(5):790–8.

[28] Bao G, Suo Z. Remarks on crack-bridging concepts. Appl Mech Rev 1992;24:355–66.

[29] Cox BN, Marshall DB. Concepts for bridged cracks in fracture and fatigue. Acta Metall Mater 1994;42(2):341–63.

[30] Hillerborg A, Modeer M, Petersson PE. Analysis of crack formation and crack growth in concrete by means of fracture mechanics and finite elements. Cement Concrete Res 1976;6:773–82.

[31] Li VC, Wang Y, Backer S. A Micromechanical model of tension-softening and bridging toughening of short random fiber reinforced brittle matrix composites. J Mech Phys Solids 1991;39:607–25.

[32] Rose LRF. Crack reinforcement by distributed springs. J Mech Phys Solids 1987;34:383–405.

[33] Suo Z, Bao G, Fan B. Delamination *R*-curve phenomena due to damage. J Mech Phys Solids 1992;40(1):1–16.

[34] Cox BN, Lo CS. Load ratio, notch, and scale effects for bridged cracks in fibrous composites. Acta Metall Mater 1992;40:69–80.

[35] Cox BN. Extrinsic factors in the mechanics of bridged cracks. Acta Metall Mater 1991;39:1189–201.

[36] Barenblatt GI. The mathematical theory of equilibrium cracks in brittle fracture. In: Dryden HL, Von Karman T, editors. Advances in applied mechanics. New York: Academic Press; 1962. p. 55–129.

[37] Dugdale DS. Yielding in steel sheets containing slits. J Mech Phys Solids 1960;8:100–4.

[38] Sneddon IN, Lowengrub M. Crack problems in the classical theory of elasticity. NewYork: Wiley; 1969.

[39] Carpinteri A, Massabò R. Bridged versus cohesive crack in the flexural behavior of brittle matrix composites. Int J Fract 1996;81:125–45.

[40] Yang QD, Cox BN. Cohesive models for damage evolution in laminated composites. Int J Fract 2005;133:107–37.

[41] Currey JD. Mechanical properties of vertebrate hard tissues. Proc Inst Mech Eng 1998;212H:399–412.

[42] Reilly DT, Burstein AH. The elastic and ultimate properties of compact bone tissue. J Biomech 1975;8:393–405.

[43] Ashman RB, Cowin SC, Van Buskirk WC, Rice JC. A continuous wave technique for the measurement of the elastic properties of cortical bone. J Biomech 1984;17:349–61.
[44] Yamada H. Strength of biological materials. Baltimore: Williams and Wilkins; 1970.
[45] Fung YC. Biomechanics: mechanical properties of living tissues. New York: Springer; 1993.
[46] Akkus O, Adar F, Schaffler MB. Age-related changes in physico-chemical properties of mineral crystals are related to impaired mechanical function of cortical bone. Bone 2004;34(3):443–53.
[47] Yang QD, Cox BN, Nalla RK, Ritchie RO. Re-evaluating the toughness of human cortical bone. Bone 2005, in press.
[48] Rice JR. The mechanics of earthquake rupture. In: International school of physics "E. Fermi", course 78. Italian Physical Society/ North Holland Publishing Company; 1980.
[49] Massabò R, Cox BN. Concepts for bridged mode II delamination cracks. J Mech Phys Solids 1999;47:1265–300.
[50] Budiansky B, Hutchinson JW, Evans AG. Matrix fracture in fiber reinforced ceramics. J Mech Phys Solids 1986;34(2):167–89.
[51] Rose LRF. A cracked plate repaired by bonded reinforcement. Int J Fract 1982;18:135–44.
[52] Lawn BR. Fracture of brittle solids. Cambridge, UK: Cambridge University Press; 1993.
[53] Rice JR. A path-independent integral and the approximate analysis of strain concentration by notches and cracks. J Appl Mech 1968; 35:379.
[54] Bazant ZP, Planas J. Fracture and size effect in concrete and other quasibrittle structures. Boca Raton, FL: CRC Press; 1998.
[55] Carpinteri A, editor. Nonlinear crack models for nonmetallic materials. Kluwer Academic Publishers: Dordrecht; 1999.
[56] Cook RF, Fairbanks CJ, Lawn BR, Mai Y-W. Crack resistance by interfacial bridging: its role in determining strength characteristics. J Mater Res 1987;2:345–56.
[57] Cox BN, Marshall DB. The determination of crack bridging forces. Int J Fract 1991;49:159–76.
[58] Massabò R, Mumm DR, Cox BN. Characterizing mode II delamination cracks in stitched composites. Int J Fract 1998;92:1–38.
[59] Sih GC, Paris PC, Irwin GR. On cracks in rectilinearly anisotropic bodies. Int J Fract Mech 1965;1:189–203.
[60] Cox BN, Lo CS. Simple approximations for bridged cracks in fibrous composites. Acta Metall Mater 1992;40(7):1487–96.
[61] Piggott MR. Load bearing fibre composites. Oxford: Pergamon; 1980.
[62] Mura T. Micromechanics of defects in solids. The Hague: Martinus Nijhoff; 1982.
[63] Cox BN, Marshall DB. Stable and unstable solutions for bridged cracks in various specimens. Acta Metall Mater 1991;39:579–89.
[64] Luo HA, Ballarini R. The effects of anisotropy on the nonlinear behaviuour of bridged cracks in long strips. J Mech Phys Solids 1994;42(2):141–57.
[65] Tada H. The stress analysis of cracks handbook. St. Louis, MO: Paris Productions; 1985.